Origin of the magnetic field enhancement of the spin signal in metallic nonlocal spin transport devices

A. J. Wright [1], M. J. Erickson [2], D. Bromley [1], P. A. Crowell,[2] C. Leighton,[3] and L. O'Brien [1,*]

[1]*Department of Physics, University of Liverpool, Liverpool, L69 7ZE, United Kingdom*

[2]*School of Physics and Astronomy, University of Minnesota, Minneapolis, Minnesota 55455, USA*

[3]*Department of Chemical Engineering and Materials Science, University of Minnesota, Minneapolis, Minnesota 55455, USA*

(Received 1 September 2020; revised 1 June 2021; accepted 2 June 2021; published 20 July 2021)

The nonlocal spin valve (NLSV) enables unambiguous study of spin transport, owing to its ability to isolate pure spin currents. A key principle of NLSV operation is that the "spin signal" is invariant under application of in-plane magnetic fields (above the ferromagnetic contact saturation field). Yet, for certain ferromagnet/normal metal pairings in NLSVs, an unexpected field enhancement of the spin signal occurs, presenting a challenge that has, thus far, been difficult to resolve with existing models. By correlating the extracted spin transport parameters with material, temperature, and field dependencies, in this work we identify field quenching of magnetic impurity scattering as the origin of this effect, confirmed by excellent agreement between our results and field-dependent Kondo theory. In addition to addressing this long-standing mystery, our findings highlight a potential systematic underestimation of spin transport parameters. By identifying signature field and temperature dependencies, we provide here a relatively simple means to isolate and quantify this additional relaxation mechanism.

DOI: 10.1103/PhysRevB.104.014423

I. INTRODUCTION

The controlled transport and manipulation of spins in metals offers the prospect of various technological advances in sensing, logic, and data storage. As an example, the problematic resistance scaling at low dimensions [1–3] of magnetic tunnel junctions in hard disk drive read head sensors provides a clear motivation to develop all-metal based alternatives. Efforts to further understand the flow of spins between, and relaxation within, ferromagnetic (FM) and non-magnetically-ordered metals (NMs) [4–22], thus continue to gather pace. Despite this concerted effort, key fundamental questions remain open. Among these, the impact of specific scattering sources on spin relaxation in NMs is a recurring theme [11,21,23–25], as are the origins of several field-dependent magnetoresistive effects [6,26–28]. Light metals, such as Cu and Al, offer an excellent testing ground to understand such issues. In essence, the low resistivity and spin-orbit coupling (SOC) in such metals result in relatively long spin lifetimes τ_s, where specific relaxation mechanisms can be intentionally introduced, e.g., through tuning disorder [29], doping with high SOC [30] or magnetic impurities [13], or manipulation of interfaces [31] and surfaces [8,22,23].

The nonlocal spin valve (NLSV) geometry offers a particularly simple, versatile means to probe spin transport in light metals with long τ_s [5]. Figure 1(a) shows a scanning electron microscope (SEM) image of a typical nanoscopic metallic NLSV device. In the NLSV geometry, a NM channel is contacted by two FM nanowires, FM_{inj} and FM_{det}, separated by a distance d. A charge current I, flowing from I^+ to I^- [see Fig. 1(a)] becomes spin polarized in FM_{inj}, thus injecting spins into the NM, which subsequently diffuse along the NM channel in the form of a pure spin current. The resulting spin accumulation reaching FM_{det} can be detected via the potential difference V_{NL}, that develops between FM_{det} and the NM, i.e., between V^+ and V^-, which can then be normalized by I to give a nonlocal transimpedance, $R_{NL} = V_{NL}/I$. Inevitably, in addition to the spin-accumulation signal, the measured R_{NL} also contains contributions from spurious effects, including finite current spreading [32] and thermoelectric voltages [33–36]. To mitigate their impact on measurements, the standard approach is to toggle the magnetization of the FM contacts, from parallel (P) to antiparallel (AP), with the difference between the two states, $\Delta R_{NL} = R_{NL}^{P} - R_{NL}^{AP}$, theoretically isolating only the "spin signal". Equivalently, one can explicitly calculate the background contribution from the average of the two states, as $R_b = (R_{NL}^{P} + R_{NL}^{AP})/2$. The spin signal is then given by $R_{spin} = R_{NL}^{P} - R_b$, as is the approach taken here. We note that these two approaches are mathematically equivalent, save for a factor of 2, i.e., $\Delta R_{NL} = 2R_{spin}$.

An example of the in-plane magnetic field, $H||y$, dependence of $R_{NL}(H)$ is shown in Fig. 1(b) for a Cu/Fe NLSV with $d = 750$ nm, over a moderate H range (up to 100 mT) and at a measurement temperature, $T = 5$ K. Both forward and reverse sweeps are shown, and R_{NL}^{P}, R_{NL}^{AP}, and R_b are clearly visible as the two FMs switch relative orientation. By measuring R_{spin} in devices with varying d, and fitting $R_{spin}(d, T)$ using a suitable model [15,37], key spin transport parameters may be extracted for the NM channel under investigation, particularly the characteristic NM spin diffusion length λ_N, and so τ_s, via the usual diffusion relation ($\lambda_N = \sqrt{D\tau_s}$, where D is the electron diffusivity).

*lobrien@liverpool.ac.uk

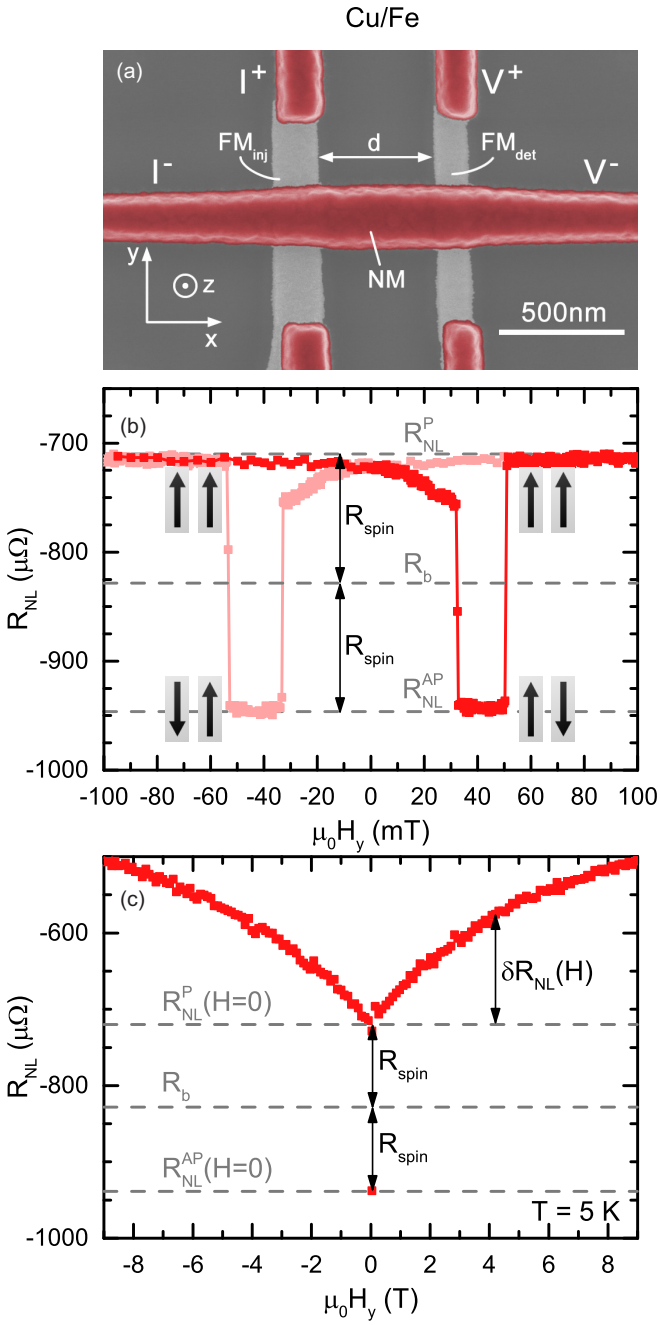

FIG. 1. (a) False color SEM image of a Cu/Fe NLSV, with the nonmagnetic metal (NM) and ferromagnetic (FM) materials highlighted. In the nonlocal geometry, a current (I) is injected at FM_{inj} and extracted from the far-left side of the NM channel, resulting in a nonequilibrium spin accumulation, manifest as a voltage (V_{NL}), measured between the far right of the NM channel and FM_{det}. (b) In-plane magnetic field (H_y) dependence of the nonlocal resistance, $R_{NL} = V_{NL}/I$, for a Cu/Fe NLSV with $d = 750$ nm, for forward (red) and reverse (pink) sweeps. The magnetization direction of the FM contacts are indicated by the arrows. $R_b = (R^P_{NL} + R^{AP}_{NL})/2$ is indicated on the figure. (c) Same as (b) up to larger (9 T) magnetic fields. Red solid squares show the measured data for parallel alignment of the FM contacts. The antiparallel response at zero field is also shown, and the definitions of R_{spin} and δR_{NL} are indicated. R^P_{NL} increases with field strength, beginning to saturate at sufficiently high fields, indicating a suppression of spin-flip scattering.

These underlying principles of operation have been essential in establishing a consistent picture of spin relaxation in NLSVs. Efforts have now largely confirmed that in nanoscopic NLSVs based on low SOC metals, relaxation is dominated by the Elliot-Yafet (EY) mechanism: [38,39] For a scattering source i (e.g., phonons, grain boundaries, impurities, etc.), $1/\tau_{s,i} = 1/\beta_i\tau_{e,i}$, where $\tau_{e,i}$ represents the momentum relaxation time due to defect type i, and β_i is the corresponding EY parameter [40]. Empirically, these rates can be summed using what is essentially Matthiessen's rule for spin transport, to give the total rate:

$$\frac{1}{\tau_s} = \sum_i \frac{1}{\beta_i \tau_{e,i}}. \tag{1}$$

While a general consensus has emerged supporting this relationship, deconvoluting contributions from specific mechanisms, i.e., determining each β_i, has been a considerable challenge, with, for example, an order of magnitude variation in measurements of the phonon contribution ($\beta_{ph} = 500-3570$) extracted from Cu NLSVs [13–15,41].

A primary source of difficulty in this regard is the surprising nonmonotonicity of $R_{spin}(T)$ [or equivalently $\Delta R_{NL}(T)$] at low T, particularly in Cu-based NLSVs [7,8,10,19,21,36]. In such devices the extracted $1/\tau_s$ is found to unexpectedly *increase* at low T, despite $1/\tau_e$ remaining essentially constant, i.e., a striking departure from naïve application of the EY model. Recent works, by ourselves and others, have shown clear evidence that this is a manifestation of the Kondo effect, originating from the presence of magnetic impurities (MIs) in the NM channel [6,13,41–46], even at very low (<100 ppm) concentrations. Additionally, we have shown that the measured spin polarization, α, is suppressed from its intrinsic value by MIs near the FM/NM interface [44]. Systematic investigation has shown that the increase in $1/\tau_s$ and suppression of α follow the expected MI concentration scaling [13,42,47–49] and logarithmic T dependence of the Kondo effect, with a characteristic temperature in good agreement with the known Kondo temperature (T_K) of the Cu/FM pairing [46]. More recently, we have also shown that Kondo spin relaxation can, surprisingly, be subsumed into an EY form, with an extremely low effective $\beta_K = 3/2$ [43,44], making MI spin relaxation highly efficient. [cf. phonon $\beta_{ph} = (740 \pm 200)$ and grain boundary $\beta_{GB} = (240 \pm 50)$ in MI-minimized NLSVs [41]].

Interestingly in the context of the above, there is surprisingly clear evidence that a (high) field enhancement of R_{NL} exists in certain (e.g., Ag/NiFe [6,26] and Cu/Fe [46]) metallic NLSVs at low T. These indications of a nonconstant $R_{spin}(H)$ are significant as they risk undermining much of the previously established knowledge of spin transport in NLSVs. Specifically, a key tenet of NLSV operation is that R_{spin} (or ΔR_{NL}) reliably measures *only* the spin signal and is, for example, field independent (when the magnetizations of the contacts are parallel to the field). Understanding the origin of this field enhancement is the main focus of this work. As an example, Fig. 1(c) shows $R_{NL}(H)$, taken under identical conditions to that of Fig. 1(b), but now over a larger applied field range of ±9 T. The field steps used here (~100 mT) are larger than the FM coercivities (<60 mT), so the low H

switching seen in Fig. 1(b) is no longer visible. The low coercivity ensures that both contacts are parallel over the entire measurement span, so we designate this curve $R_{\rm NL}^{\rm P}(H)$. $R_{\rm NL}^{\rm P}$ is clearly not constant, however, with a monotonic increase found on increasing $|H|$. $R_{\rm spin}$ is indicated schematically in Fig. 1(c), from which it is apparent that the field enhancement is *substantial* compared to the original low-field spin signal, in many cases exceeding $R_{\rm spin}$ in Cu/Fe devices. We define this field enhancement, $\delta R_{\rm NL}(H)$ as the difference between $R_{\rm NL}^{\rm P}$ at zero field and at a given field H:

$$\delta R_{\rm NL}(H) = R_{\rm NL}^{\rm P}(H) - R_{\rm NL}^{\rm P}(0). \tag{2}$$

A rigorous explanation of this low T effect has remained largely elusive. Multiple works have investigated qualitatively similar observations, but none can consistently explain all trends. The most directly comparable studies [6,26], using all-metal Ag/NiFe NLSVs, ascribe the field dependence to screening of scattering from paramagnetic MIs or magnetic clusters, due to alignment with an applied field. Correlating this picture with the T and H dependence of $R_{\rm NL}(H)$ has been problematic, however, with a lack of ideal agreement between data and models based on $S = 1/2$, Brillouin-like scaling with temperature and field.

In this work we perform an extended investigation into the field dependence of $R_{\rm NL}$ in metallic NLSVs. By varying the FM (Fe, Co, $Ni_{80}Fe_{20}$) and NM (Cu, Al) pairings, we demonstrate that the magnitude of $\delta R_{\rm NL}(H)$ is clearly linked to the ability of the NM to host MIs. In Al, where local magnetic moments are not supported on $3d$ transition metal impurities [47–49], no high-field dependence of $R_{\rm NL}$ is found. In Cu, where the effect is strong, measurements of $\delta R_{\rm NL}$ as a function of d, T, and H reveal an isotropic field dependence with a complex T and d relationship. However, taking the critical step of linking $\delta R_{\rm NL}$ to enhancement of $R_{\rm spin}$ allows us to extract values for $\lambda_N(H,T)$ and $\tau_s(H,T)$ using standard spin diffusion theory. Extending spin transport models to incorporate Kondo magnetoresistance theory, we then demonstrate excellent quantitative agreement between the experimental $1/\tau_s(H,T)$ and Kondo spin relaxation theory. A physical picture thus prevails where the application of H suppresses MI scattering, restoring the expected T dependence and magnitude of the nonlocal spin signal. As well as solving the long-standing mystery as to the origin of this low-T field enhancement effect, this high-field signature therefore acts as a convenient method to distinguish spin relaxation due to MIs in metals. We also note that failure to account for this effect can potentially significantly impact spin transport measurements and conclusions, particularly in Hanle spin precession experiments, and should thus be incorporated into future analyses.

II. SAMPLE FABRICATION AND EXPERIMENTAL DETAILS

NLSV devices were fabricated using multiangle electron beam evaporation through a suspended shadow mask. The masks consisted of a polymethylglutarimide (PMGI)/polymethyl methacrylate (PMMA) bilayer resist stack and were written using a Vistec EPBPG5000+ electron beam lithography tool, on Si/Si-N (2000 Å) substrates. FM materials were deposited at an angle of 49° normal to the plane of the device at a rate of 0.5 Å/s. NM materials were deposited normal to the plane of the device at a rate of 1.0 Å/s. Nominal purities of the FM and NM materials were 99.95% and 99.999%, respectively. All materials were deposited in the same vacuum system, with a base pressure of the order of $\sim 10^{-10}$ Torr. Deposition pressures were in the range 8×10^{-10} to 4×10^{-8} Torr. Thicknesses were calibrated using grazing incidence x-ray reflectivity and monitored during growth using quartz crystal monitors. A nucleation pad on one of the FM contacts in each device was used to assist domain wall nucleation, reducing the coercivity of that contact, making the antiparallel state more readily achievable. NM and FM thicknesses were 200 and 16 nm, respectively, for all devices, and widths ($\sim$200 nm and $\sim$100–150 nm, respectively) were obtained directly from SEM measurements. All devices were annealed at 80°C during processing [42].

Local resistivity measurements were first used to obtain the FM and NM resistivities, $\rho_{\rm FM}$ and ρ_N, and verify the transparent interface limit at the FM/NM interface. Momentum scattering rates due to defects $1/\tau_{e,\rm def}$ and phonons $1/\tau_{e,ph}$ were calculated from these resistivity measurements using $\rho_N^{-1} = \frac{1}{3}e^2 N(\varepsilon_F) v_F^2 \tau_e$, where e is the electron charge, $N(\varepsilon_F)$ the Cu density of states at the Fermi energy, and v_F the Fermi velocity, with $\rho_{\rm def}$ estimated from the 5 K data. Transport measurements were taken using a 13 Hz AC supply at bias currents from 100 μA to 1 mA. A 3 $\mu\Omega$ noise floor was present in the $R_{\rm NL}$ measurements. At high temperatures (>200 K) and large d(>1500 nm), the $R_{\rm NL}$ signal was dominated by this noise floor. An 8% uncertainty in device dimensions was also present.

III. RESULTS

A. Material dependence of $\delta R_{\rm NL}$

To date, only limited combinations of FM and NM materials (Cu/Fe [46] and Ag/NiFe [6,26]) have been tested in all-metal NLSVs at relatively high fields. Here, we expand this parameter space through NLSVs fabricated using Fe, Co, and $Ni_{80}Fe_{20}$ as the FM, and Cu or Al as the NM. The field dependence of $\delta R_{\rm NL}$ for different material combinations is shown in Fig. 2 and represents a key result of our work. Data are shown here for devices with $d = 250$ nm, at $T = 5$ K and, for direct comparison, they are normalized by $R_{\rm spin}$ in order to compensate for differences in, e.g., FM current polarization α, and FM (NM) resistivity $\rho_{\rm FM}$ (ρ_N), etc. We first highlight the Cu/Fe case (red squares). These are the equivalent data to those in Fig. 1(c), once again showing a monotonic increase in $\delta R_{\rm NL}/R_{\rm spin}$ up to the largest fields accessible ($\mu_0 H = 9$ T). Inspection across all other samples shows an approximately similar curve shape to these Cu/Fe data, with $\delta R_{\rm NL}$ monotonically rising, well beyond the saturation magnetization M_s of the respective FMs ($M_s < 2$ T in all cases, ruling out FM contact rotation as a contributing factor). Comparing devices, however, clear differences in the normalized magnitude of $\delta R_{\rm NL}$ are evident. Looking first at the Cu/Co, Cu/Fe, and Cu/$Ni_{80}Fe_{20}$ devices, it is clear that a large variation in $\delta R_{\rm NL}/R_{\rm spin}$ occurs across the choice of FM materials. Equally, considering Cu/Fe and Al/Fe, a noticeable

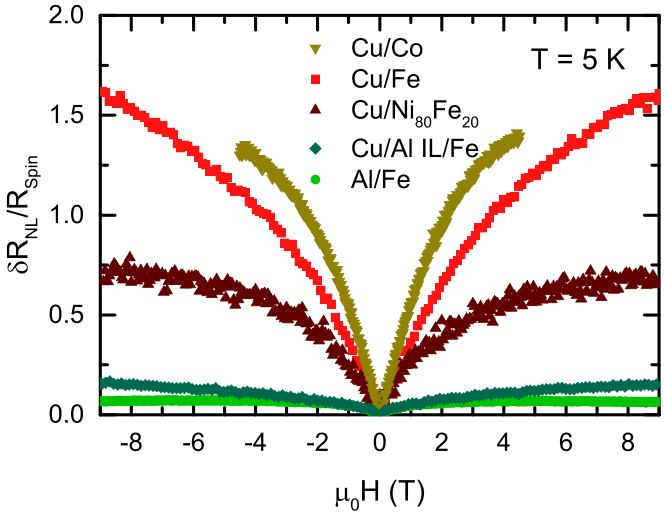

FIG. 2. (Normalized) $\delta R_{\rm NL}/R_{\rm spin}$ as a function of in-plane applied magnetic field, for various materials. Devices shown have $d = 500$ nm except for Cu/Co and Cu/$Ni_{80}Fe_{20}$ which have $d = 400$ nm. Measurements of Cu/Co were taken only up to an applied field of $\mu_0 H = \pm 4.5$ T. The effect of in-plane applied magnetic field is most prominent for Cu/Co and Cu/Fe. For Cu/Al IL/Fe and Al/Fe, the effect is almost negligible.

dependence on the choice of NM material is found: whereas a large $\delta R_{\rm NL}/R_{\rm spin}$ is seen in Cu/Fe devices, almost no field dependence is observed for Al/Fe. The $\delta R_{\rm NL}/R_{\rm spin}$ behavior is thus dependent on *both* the FM *and* NM material choices.

Similar field-dependent trends are also found in other spintronic devices, including three terminal spin valve measurements of semiconductors [50], hydrogenated graphene NLSVs [51], and heavy metal magnetoresistance measurements [52], attributed to precession from inhomogeneous magnetostatic fields, local moment exchange interactions, or Hanle precessional magnetoresistance, respectively. In the case of light metal NLSVs, the nonlocal measurement (limiting the impact of contact relaxation), metallic nature of the transport, extended field dependence (>9 T), and low SOC (and spin Hall angle) rule out each of these explanations.

Instead, as with earlier work on MI effects in spin transport, we return to the stark correlation between the ability of the host NM to support MIs arising from the FM, and (in this case) the magnitude of $\delta R_{\rm NL}(H)$. Specifically, Cu readily hosts local magnetic moments on dissolved $3d$ transition metal impurities, whereas Al (primarily due to its high Fermi level) does not [47–49], a trend that is precisely reflected in the magnitudes observed in Fig. 2. This is further supported by $\delta R_{\rm NL}/R_{\rm spin}$ in Al interlayer (Al IL) devices, where a thin (∼5 nm) layer is deposited between the Cu and Fe layers. Due primarily to the low diffusivity of Fe in Al, the Al IL greatly reduces the concentration of Fe impurities in the channel. As a consequence, Cu/Al IL/Fe devices exhibit a weak (but nonzero) high-field dependence.

B. Determining the origin of $\delta R_{\rm NL}$

A natural implication of this correlation between local moment formation and the high-field dependence is that $\delta R_{\rm NL}$ arises from a spin transport effect, related to MI-driven spin relaxation. Before continuing with a MI-based analysis, including detailed comparison between data sets, we first consider other potential phenomena, unrelated to spin transport, as the potential origins of $\delta R_{\rm NL}(H)$, e.g., field-dependent thermoelectric [33,34,53] or current spreading [32] effects. In such cases, $\delta R_{\rm NL}$ would be expected to correlate broadly with the field-independent background $R_b = (R^{\rm P}_{\rm NL} + R^{\rm AP}_{\rm NL})/2$, in sign, magnitude, d, or T dependence.

To test this, in Figs. 3(a) and 3(b), we show the temperature evolution of $\delta R_{\rm NL}$ and R_b for Cu/Fe NLSVs of varying d, and provide a direct comparison of the two in Fig. 3(d). Examining Figs. 3(a) and 3(b), we note that the magnitude of $\delta R_{\rm NL}$ is relatively large, at times exceeding that of R_b and $R_{\rm spin}$ [shown in Fig. 3(c)]. Field-dependent corrections to R_b from current spreading, of order $\omega_c \tau_e$ (where ω_c is the cyclotron frequency) [32], are weak in comparison [at most of the order 10^{-2} at 9 T for our longest measured $\tau_e \approx 50$ fs ($T = 5$ K)] [32], ruling out current spreading as the origin of $\delta R_{\rm NL}$. Further examining Figs. 3(a) and 3(b), it is also clear that there is no correlation between the evolution of $\delta R_{\rm NL}$ and R_b: Whereas $\delta R_{\rm NL}$ decreases with both increasing T and d [Fig. 3(a)], R_b appears largely independent of these parameters in Cu/Fe [Fig. 3(b)]. Comparing different materials pairings (as shown in Supplemental Material Fig. S1 [54]) yields further inconsistencies in the signs and magnitudes of $\delta R_{\rm NL}$ and R_b, which are incompatible with the possibility that $\delta R_{\rm NL}$ arises from current spreading or thermoelectric effects. Thus, we can convincingly rule out contributions from conventional (nonspin) transport phenomena, which otherwise determine R_b.

We next consider magnetothermoelectric (e.g., a field-dependent spin Seebeck contribution), or weak (anti)localization effects, which are anisotropic with respect to the applied field direction [27]. Comparing $R_{\rm NL}(H)$ for different field directions, as in Fig. 3(f), $\delta R_{\rm NL}(H)$ is found to be isotropic with respect to the direction of the applied field. Here, we compare $R_{\rm NL}(H)$ for in-plane (H_y) and out of plane (H_z) magnetic fields at $T = 5$ K (other temperatures are shown in Supplemental Material Fig. S2 [54]). Out of plane measurements are shown for initial parallel and antiparallel alignment of the FM contacts, and are essentially Hanle effect measurements: The oscillations in $R_{\rm NL}$ thus arise from Larmor precession of conduction electron spins about H_z, decaying as the magnetizations of $\rm FM_{inj}$ and $\rm FM_{det}$ rotate to align with the field. These in-plane and out of plane measurements were taken at different times, and inevitably there is a small difference in the zero-field offset to $R_{\rm NL}$. For ease of comparison, the offset in the in-plane measurements has been shifted (by ∼30 μΩ), to match that of the parallel, out of plane measurement at zero field. Beyond the saturation field of the FM contacts (1.8 T), the out of plane $R_{\rm NL}$ for both parallel and antiparallel orientations increases exactly as the in-plane $R_{\rm NL}$ does. This is to say that $\delta R_{\rm NL}(H)$ is independent of the direction of the applied field, and therefore does not originate from magnetothermoelectric, weak (anti)localization effects, nor current spreading, which would all have an anisotropic dependence on field direction [27,28].

In contrast, for a given NM/FM pairing, we find that $\delta R_{\rm NL}(\mu_0 H = 9\ {\rm T})$ broadly scales with the magnitude of $R_{\rm spin}$

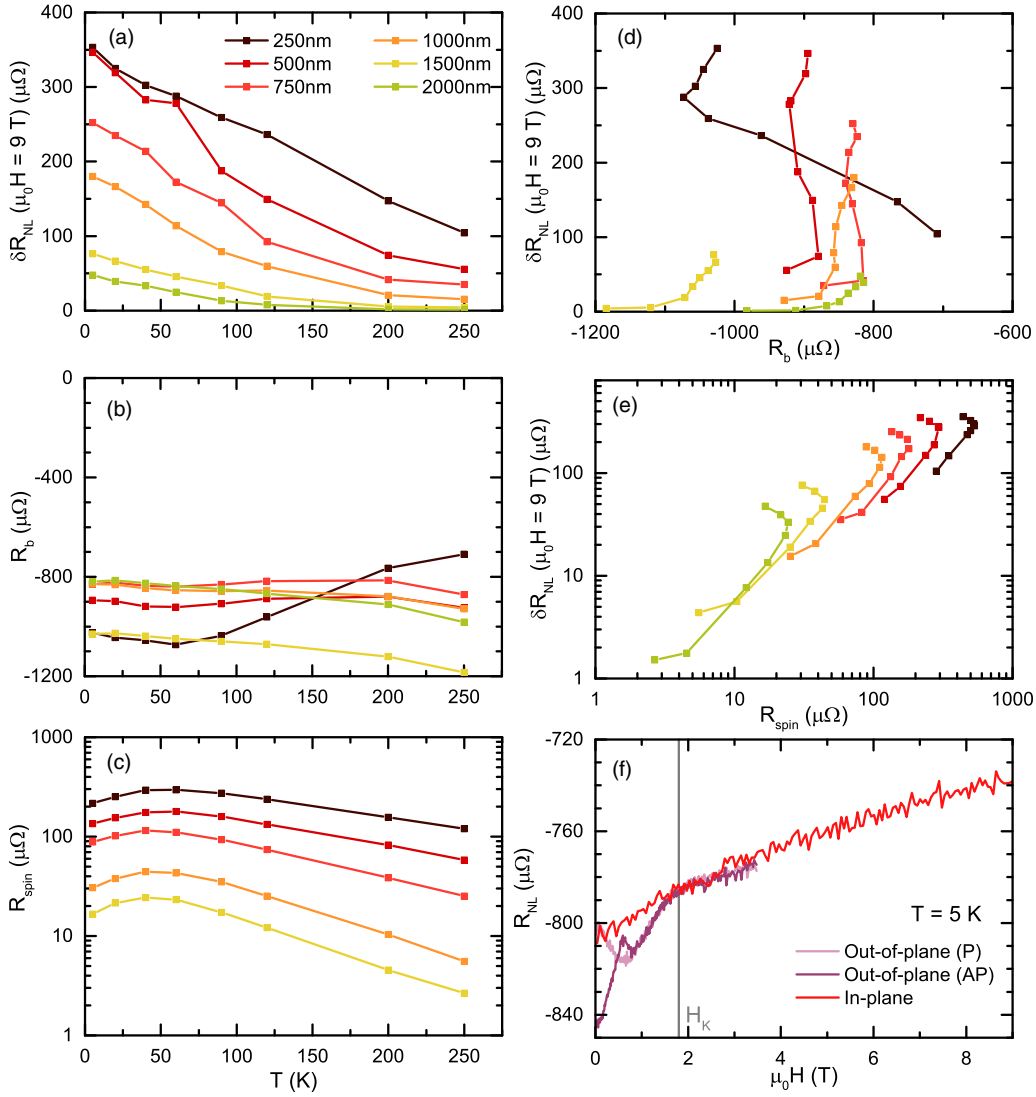

FIG. 3. Temperature evolution of (a) $\delta R_{\rm NL}(\mu_0 H = 9\ T)$, (b) R_b, and (c) $R_{\rm spin}$ for Cu/Fe NLSVs of various d. (d) Direct comparison of $\delta R_{\rm NL}(\mu_0 H = 9\ T)$ and R_b, demonstrating no correlation between the two parameters, hence ruling out background effects as the origin of $\delta R_{\rm NL}$. (e) $\delta R_{\rm NL}(\mu_0 H = 9\ T)$ as a function of $R_{\rm spin}$. A clear, consistent correlation exists between the two, highlighting that $\delta R_{\rm NL}$ arises from spin-transport related effects. (f) Field enhancement of $R_{\rm NL}$ for in-plane and out-of-plane (Hanle) measurements for a $d = 2000$ nm Cu/Fe NLSV at 5 K. Beyond the saturation field (H_K) of the FM contacts (vertical gray line) the in-plane and out of plane field responses of $R_{\rm NL}$ are identical, indicating that $\delta R_{\rm NL}$ is independent of applied field direction.

(see Figs. 3(a), 3(c), and 3(e) for Cu/Fe, and Supplemental Material Fig. S1 [54] for Cu/Co, Cu/$Ni_{80}Fe_{20}$, and Al/Fe). While the specific dependence of $\delta R_{\rm NL}(T, d)$ is complex, and $\delta R_{\rm NL}/R_{\rm spin}$ varies between pairings, for a given FM and NM, $\delta R_{\rm NL}(H)$ decreases on reduction of $R_{\rm spin}$, either through increasing T or d [Fig. 3(e)]. From this we conclude that $\delta R_{\rm NL}(H)$ has a similar dependence on the spin-dependent parameters of each material, and indeed arises from a pure spin transport effect.

We next examine the T dependence of $\delta R_{\rm NL}(H)$. Cu/Fe offers one of the largest field enhancements, and so we focus on this pairing. (Cu/Fe also provides a convenient pairing for testing Kondo-related contributions, due to its relatively high miscibility and an easily accessible $T_K = 30$ K [47]). Figure 4 displays $\delta R_{\rm NL}(H)$ for a Cu/Fe device with $d =$ 250 nm, across a T range of 5–250 K. As well as increasing with field, $\delta R_{\rm NL}$ clearly decreases with increasing T. Qualitatively, such scaling is commensurate with the saturation of paramagnetic MI moments under increasing field or decreasing temperature. However, plotting the normalized $\delta R_{\rm NL}$ vs $\mu_B\mu_0 H/k_B T$ (inset) fails to collapse the data onto a single functional form, as might be anticipated for the response of free moments under field. Furthermore, $\delta R_{\rm NL}$ shows a $\mu_B\mu_0 H/k_B T$ dependence that is not only far stronger than expected for $S = 1/2$ MIs, (for all but the lowest 5 K data) but is also poorly described by a classical Langevin expression, where the fitted J varies dramatically with T (see Supplemental Material Fig. S3 [54]). A similar observation was made in Refs. [6,26], and was attributed to the finite magnetic shape anisotropy energy of clustered MIs. In our devices similar $\delta R_{\rm NL}(H)$ is observed across different material pairings; therefore analysis based on magnetic shape anisotropy would

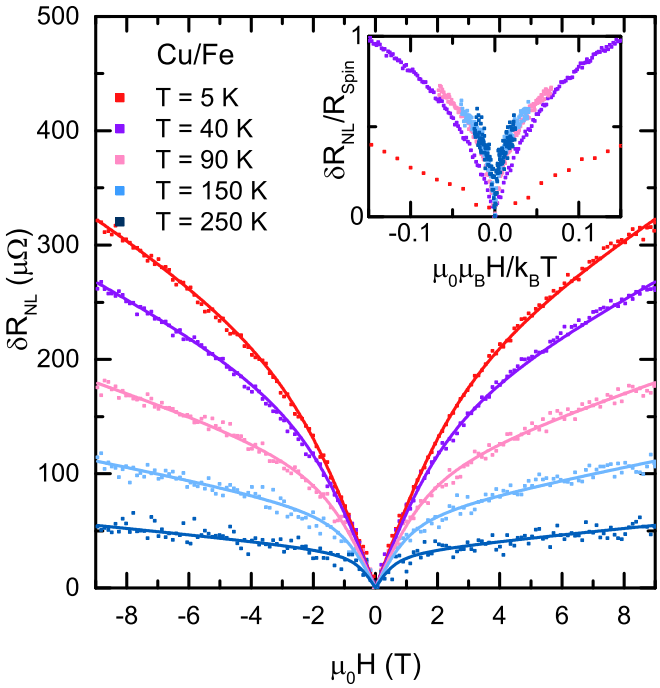

FIG. 4. $R_{\rm NL}$ as a function of $\mu_0 H$ for a Cu/Fe NLSV with d = 500 nm , at various temperatures. Solid lines are fits using Eq. (3), in order to model the data as a continuous function of field. Inset shows $\delta R_{\rm NL}$ normalized to $R_{\rm spin}$ as a function of $\mu_0\mu_B H/k_B T$ for the same device. The 5 K data extend beyond the range of the plot. The data clearly do not collapse onto a single form, indicating that the field enhancement is not simply due to alignment of magnetic impurities.

require similar clustering of MIs across these pairings. However, the range of thermodynamic solubilities is unlikely to produce identical distributions and precipitations of (potentially clustered) MIs, seeming to disfavor such a model, and suggesting a fundamentally different mechanism is at play.

C. Extracting spin transport characteristics

Acknowledging that $\delta R_{\rm NL}$ arises from a spin transport effect, we must accept that any changes in $\delta R_{\rm NL}(T)$ are manifestly convolved with the T-dependent variation of the key relevant NLSV material parameters, particularly $\tau_s(T)$, $\alpha(T)$, $\rho_N(T)$, and $\rho_{\rm FM}(T)$. Given that all other key parameters are either constant (d, and the NM thickness t_N) or have a weak H dependence (ρ_N, $\rho_{\rm FM}$, λ_F), we proceed by considering the (MI) scattering contribution to τ_s and α, which are now anticipated to depend on H, as well as T. To extract these terms, a comprehensive study of $R_{\rm NL}(H)$ in Cu/Fe NLSVs was performed at various d (250–2000 nm) and T (5–250 K).

Reasoning that the field dependence of $R_{\rm NL}$ can be subsumed into τ_s and α is equivalent to defining a field-dependent NLSV spin signal, $R_{\rm spin}(H) = R_{\rm spin}(0) + \delta R_{\rm NL}(H)$, where $R_{\rm spin}(0) = R^{\rm P}_{\rm NL}(0) - R_b$ as defined earlier. This model is based on the assumption that R_b is independent of the magnetic field, which is easily verified following our discussion in Sec. III B. To calculate $R_{\rm spin}(H)$, we obtained $\delta R_{\rm NL}(H)$ data for a range of T and d values, via Eq. (2). Because it is convenient to be able to represent the data as a continuous function of H, we adopt for now a purely empirical fitting function:

$$\delta R_{\rm NL}(H) = \left| A_1\left(\coth x - \frac{1}{x}\right)\right| - A_2|\mu_0 H|, \qquad (3)$$

where $x = \mu_0(H - H_0)/b$, and A_1, A_2, b, and H_0 are constant fitting parameters. We emphasize that our use of Eq. (3) is solely as a representation of the data, and offers little physical insight. The fitted curves (shown by the solid lines in Fig. 4) are combined with measurements of $R_{\rm spin}(0)$ to obtain $R_{\rm spin}(H)$ for any given field within ±9 T, and at selected d = 250–2000 nm and T = 5–250 K. Representative values of $R_{\rm spin}(d, H)$ are shown in Fig. 5(a) for $\mu_0 H$ = 0, 1, 3, 5, and 9 T, at T = 5 K. Despite the varying magnitude of $\delta R_{\rm NL}$ vs H, T, and d, $R_{\rm spin}(d, H)$ assumes the expected functional form for all H: a simple exponential decay at high d with the deviation at low d that is a hallmark of NLSV spin diffusion in the low interface resistance limit. Encouraged by this d dependence, we fit these data using a standard one-dimensional (1D) magnetoelectronic circuit theory solution for $R_{\rm spin}(H)$, applied to the NLSV geometry in the transparent interface limit [55]:

$$R_{\rm spin}(H) = 2\frac{\alpha^2_{\rm eff}R^2_F}{(1-\alpha^2_{\rm eff})^2 R_N}\,\frac{\exp\left(-\frac{d}{\lambda_N}\right)}{\left[1+\frac{2R_F}{(1-\alpha^2_{\rm eff})R_N}\right]^2 - \exp\left(-\frac{2d}{\lambda_N}\right)}. \qquad (4)$$

Here, $R_N = \rho_N\lambda_N/w_N t_N$ and $R_F = \rho_F\lambda_F/w_F w_N$ are the NM and FM spin resistances, with ρ_N (ρ_F) and w_N (w_F) the respective resistivities and widths; t_N is the NM thickness. In Eq. (4) we employ an effective spin polarization $\alpha_{\rm eff}$ to account for the presence of MI-induced depolarization at the NM/FM interfaces [42] and to distinguish it from the intrinsic FM polarization α. To constrain the fitting, we experimentally measure ρ_N on the same NLSVs, and ρ_F on nanowires of identical cross-sectional dimensions. All dimensions were measured using SEM for each device, and λ_F was constrained to a value of 4 nm through empirical scaling with ρ_F [46,56]. Only λ_N and $\alpha_{\rm eff}$ thus remain as fitting parameters, and these two are readily separable through the high-d exponential dependence, which is determined only by λ_N. Extracted values of $\lambda_N(T)$ for selected field values are shown in Fig. 5(b), along with the corresponding $1/\tau_s(T)$ (through the diffusion relation $\lambda_N = \sqrt{D\tau_s}$) in Fig. 5(c). In Fig. 5(d) the relevant $\alpha_{\rm eff}(T)$ are displayed.

D. Temperature and field dependence of spin transport

Looking first at the zero-field $\lambda_N(T)$ data in Fig. 5(b), an initial increase in λ_N with decreasing T is observed from 250 to 40 K, as phonon scattering is progressively frozen out. Below 40 K a noticeable downturn is then observed, producing a peak in $\lambda_N(T)$. This peak, widely seen in other works [7,8,11,21], and clearly contrasting with the naïvely expected (monotonic) EY-like behavior [40,57], is qualitatively similar to that seen in low-purity Cu/Fe NLSVs [41,42,46]. There, it is attributed to Kondo relaxation arising from dilute MIs, present throughout the channel (even in initially high-purity NM materials, NM/FM interdiffusion will inevitably introduce MIs into the channel if the solubility is high enough). We note that, at low T, λ_N should approach a constant value

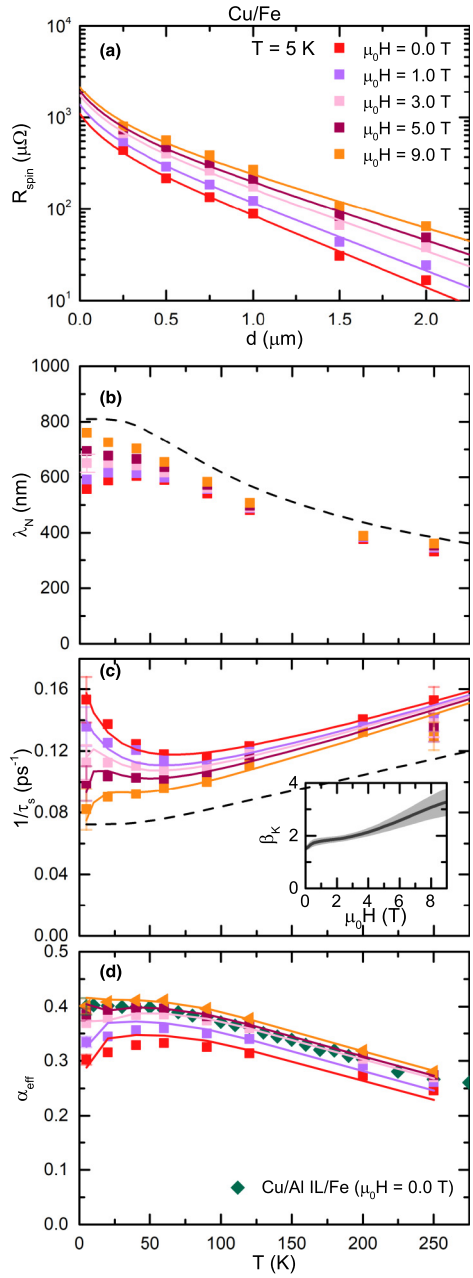

FIG. 5. Data from measurements of Cu/Fe devices. For clarity, only select field strengths are shown, although a continuous range was available to us. (a) Variation of $R_{\text{spin}}(H)$ with d. Error bars are smaller than the symbol size. Solid lines are fits to the data using Eq. (4). (b) Spin diffusion length (λ_N) in the NM channel as a function of temperature. The dashed line is an estimate of the spin diffusion length from phonon and impurity scattering only. Error bars are smaller than the symbol size. (c) Same as (b) but for spin-flip scattering rate ($1/\tau_s$). Solid lines are fits using Eqs. (1) and (6). For clarity, error bars are only shown for the first data points and last data points. (Inset) Quasicontinuous variation of β_K with field strength from fitting of data in (c). The light gray shaded area represents the uncertainty in the fit values. (d) Effective spin polarization α_{eff} as a function of temperature. The zero-field and high-field (9 T) data are shown for a Cu/Fe device. Data from a Cu/Al IL/Fe device at zero field are also shown for comparison. Both devices have $d = 500$ nm. Under a high field, α_{eff} for the Cu/Fe closely follows that of the Cu/Al IL/Fe device, indicating that "normal" behavior has been restored.

due to the unitary limit of Kondo relaxation. As shown in our previous work, this is readily observed in our devices when $T \ll 30$ K [46], and is particularly prevalent in devices with high MI concentrations and/or higher Kondo temperatures [42,45]. Indeed this effect is also evident here, although the coarser T steps limit quantitative comparison.

Although on first inspection the downturn in $\lambda_N(T)$ is a seemingly weak effect, we emphasize that the full impact of MI relaxation can only be assessed from the departure from conventional spin relaxation due to phonon and T-independent defect scattering alone. To demonstrate this, we estimate the expected $1/\tau_s(T)$ and $\lambda_N(T)$ for EY-type scaling, using Eq. (1) for phonon and defect scattering. $1/\tau_{e,\text{def}}$ and $1/\tau_{e,ph}$ are calculated as described in Sec. II, and we use typical values for phonon and defect EY parameters, $\beta_{ph} = 740$ and $\beta_{\text{def}} = 240$, respectively, previously determined from devices in which MI effects were minimized [41]. (Under such conditions, grain boundaries were found to dominate defect scattering, and so we use $\beta_{\text{def}} = \beta_{\text{GB}}$.) λ_N values were then calculated from $1/\tau_s$ using the diffusion relation $\lambda = \sqrt{\tau D}$, where D is the diffusivity taken from local resistivity measurements. The corresponding curve, represented by the black dashed line in Fig. 5(b), demonstrates the stark impact of MI spin relaxation, which results in ~30% suppression of λ_N at 5 K. In this context, the impact of applying H becomes clearer. Specifically, examining $\lambda_N(T)$ with increasing H we find a simple trend where $\lambda_N(T)$ steadily rises until it approaches the very same monotonic dependence expected in Kondo-minimized devices. We conclude, therefore, that the field acts to quench T-dependent MI (i.e., Kondo) scattering.

Equivalent behavior is observed in $1/\tau_s$, as shown in Fig. 5(c), where the $H = 0$ scattering rate initially decreases with T, down to 90 K, before unexpectedly increasing on further cooling. Both the magnitude and T dependence of this behavior are in good agreement with the $1/\tau_s$ seen in other Cu/Fe devices [41,42,46], but once again strongly contrast with expected EY theory (black dashed curve). At this point we note that in the Kondo model, T_K determines a characteristic temperature scale about which the scattering rate becomes enhanced, rather than any critical temperature. The increase in $1/\tau_s$ about $T \sim 25$ K is therefore consistent with the onset of the Kondo effect in Cu/Fe ($T_K = 30$ K) [46,47,58]. While this upturn in $1/\tau_s$ at low T has now been widely observed, the restoration of $1/\tau_s$ under increasing H is stark. Under application of the field, $1/\tau_s$ approaches the expected EY dependence, which is nearly restored by $\mu_0 H = 9$ T. Despite the action of H in quenching Kondo scattering, a noticeable shoulder remains at low T, even at $\mu_0 H = 9$ T. As we will detail below, this shoulder is a hallmark of such MI scattering, and is produced by the competition between different energy scales in the system, notably the Kondo singlet, thermal, and Zeeman energies.

We next consider these observations further by comparing Cu/Fe with other NM/FM combinations. While we do not make an in-depth quantitative comparison, we do examine the (normalized) residual scattering rate, $1/\tau_{s,\text{ res}} = 1/\tau_s^{\text{zero field}} - 1/\tau_s^{\text{high field}}$, for Cu/Co, Cu/NiFe, and Cu/Fe, where "high field" refers to the highest field available (4.5 T for Cu/Co, 9 T otherwise) (see Supplemental Material [54]). From the preceding discussion, in essence, $1/\tau_s^{\text{high field}}$ corresponds to

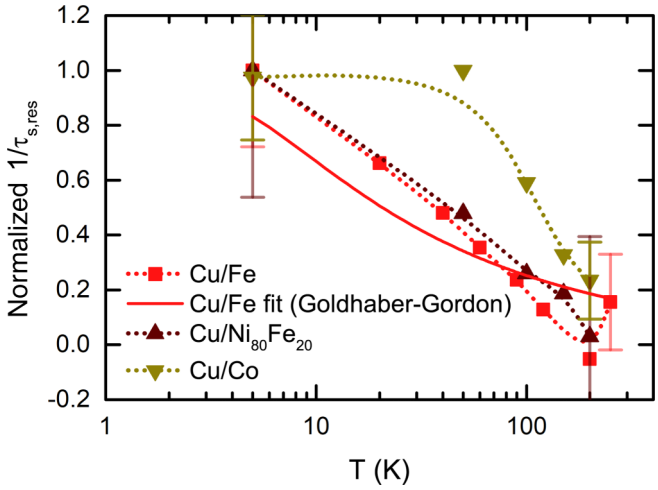

FIG. 6. Normalized residual spin relaxation rate ($1/\tau_{s,\mathrm{res}} = 1/\tau_s^{\text{low field}} - 1/\tau_s^{\text{high field}}$) as a function of temperature ($\log_{10}$ scale), for Cu/Co, Cu/Fe, and Cu/$Ni_{80}Fe_{20}$. The Cu/Fe data are fit using the phenomenological Goldhaber-Gordon expression of Eq. (5) (solid, red line). The Cu/Co and Cu/$Ni_{80}Fe_{20}$ data sets are incomplete and so should be treated only qualitatively. For these data, a guide to the eye (dotted line) is given. For clarity, error bars for only the first and last data points are shown.

the relaxation rate under the near-complete quenching of MI scattering, but without any changes to $1/\tau_{s,ph}$. Defined in this way, $1/\tau_{s,\mathrm{res}}(T)$ can therefore provide an estimate of the T dependence of MI scattering, although it cannot give insight into its overall magnitude. Additionally, the absolute value of $1/\tau_{s,\mathrm{res}}$ is dependent on the material properties of the FM/NM pairings, and so, for suitable comparison between pairings, we normalize the data to their maximum value.

The normalized $1/\tau_{s,\mathrm{res}}(T)$ data are shown in Fig. 6, on a logarithmic temperature scale. In all cases, as expected, $1/\tau_{s,\mathrm{res}}$ decreases with temperature. Significantly, Cu/Fe shows a clear logarithmic T dependence about a temperature range consistent with $T_K = 30$ K. As this data set is quite complete, we fit the data using the phenomenological Goldhaber-Gordon expression for Kondo scattering [59]:

$$\frac{1}{\tau_{s,\mathrm{res}}} = G_0\left[\frac{T_K'^2}{T^2 + T_K'^2}\right]^s \tag{5}$$

where $T_K' = T_K\sqrt{2^{1/s} - 1}$ and $s = 0.22$ for spin-1/2 MIs [46,59]. Since the data are normalized, we fix $G_0 = 1$ and T_K remains as the only free parameter. The fit (solid line) models the data reasonably well, returning $T_K = (20 \pm 8)$ K, in decent agreement with the expected $T_K = 30$ K. Encouragingly, this Cu/Fe behavior is reproduced in Cu/$Ni_{80}Fe_{20}$ (Ni is not expected to show any Kondo contribution due to the prohibitively high $T_K \sim 1000$ K; thus only Fe moments should contribute for Cu/$Ni_{80}Fe_{20}$). In contrast, Cu/Co has a response which is clearly shifted to higher T, appearing to reach the unitary limit at $T \sim 50$ K. This correlates well with the increased T_K value for this pairing (Cu/Co has a T_K of either 23 or 500 K depending on whether the MIs are surface or bulk, respectively [46,60]), further cementing the relationship between $\delta R_{\mathrm{NL}}(H)$, through $1/\tau_s$, and MI scattering.

E. Fitting the spin relaxation rate, $1/\tau_s$

Given the success of Kondo scattering in qualitatively describing $1/\tau_s(T)$ for Cu/FM NLSVs, we continue this approach, now quantitatively accounting for the impact of H on $\tau_{s,K}$. Previous studies of the magnetoresistance of $Cu_{1-x}Fe_x$ and similar alloys have shown that application of a magnetic field indeed suppresses Kondo scattering at low temperatures [61,62], and several qualitatively similar models have been proposed [63–65]. Here, we use the model derived by Litvinov [63], which most accurately represents Fe impurities in a metallic host. (We have also performed analysis using the Abrikosov model [64], which we present in the Supplemental Material Fig. S4; similar results are produced [54].) In the Litvinov theory, the Kondo momentum scattering rate is given by

$$\frac{1}{\tau_{e,K}} = \frac{3\pi c J^2}{32\hbar\varepsilon_F}\frac{2\tanh\left(\frac{Q}{k_BT}\right) - \tanh\left(\frac{Q}{2k_BT}\right)}{\sinh\left(\frac{Q}{k_BT}\right)} \times \left\{1 + \frac{3J}{4\varepsilon_F}\ln\left[\frac{k_BT_K^2}{(2k_BT)^2 + Q^2}\right]\right\}^{-2} \tag{6}$$

where c is the concentration of magnetic impurity atoms, J is the exchange energy between the magnetic impurity and conduction electrons, and ε_F is the Fermi energy. $Q = \mu_0\mu_B g_i H$ is the Zeeman energy due to the magnetic field, where g_i is the impurity g factor (assumed to equal 2). There are two energy scales at play in this equation: The first, which comprises the hyperbolic terms, describes the magnetization of the magnetic impurities and the competition between T and H; the second, which is the modified Kondo term, acts to suppress the scattering rate, with contributions from the singlet and Zeeman energies.

The data in Fig. 5(c) were fit using Eqs. (1) and (6), considering terms from phonon, T-independent impurities, and Kondo scattering explicitly. Here, $1/\tau_{e,ph}$ and $1/\tau_{e,\mathrm{imp}}$ are known from local measurements of ρ_N, while $J = -0.91$ eV and $\varepsilon_F = 7.0$ eV may be constrained for Fe [44,61]; $\beta_K = 3/2$ is known at zero field [44,66]. At $H \neq 0$, however, β_K is expected to vary: The Zeeman energy of the magnetic field breaks the symmetry of spin-flip Kondo scattering, but not of spin-conserving Kondo scattering, resulting in different field dependencies and hence a nonconstant $\beta_K(H)$ [65,67,68]. As discussed further below, the fits therefore remain underconstrained, with free parameters β_{def}, β_{ph}, c, and $\beta_K(H)$. For simplicity, we have employed a constant, volume average impurity concentration in the model, although it is expected that c will vary with distance from the NM/FM interface [42]. Since $\beta_K(H = 0) = 3/2$, the zero-field data were first fit, returning values of $\beta_{\mathrm{def}} = 230$, $\beta_{ph} = 470$, and $c = 890$ ppm. From the earlier discussion, these values are clearly physically reasonable, and fall among those from our prior work, and the work of others [9,11,15,18,41]. As these parameters are expected to be invariant under H, they were then used as fixed values for the remaining fits, with only $\beta_K(H)$ allowed to vary, significantly constraining the fit. Best fit curves using this approach are shown at select fields by the solid lines in Fig. 5(c), and the variation of the extracted $\beta_K(H)$ is displayed in the inset.

It can be clearly seen that this model represents the data well; in particular, the knee observed between $T = 5$ and 50 K at higher fields is accurately reproduced. This is a strong indication that the magnetic field is indeed acting to suppress Kondo scattering in the NM channel, and that the high-field dependence of $R_{\rm spin}(H)$ can be quantitatively understood through the quenching of the (T-dependent) singlet scattering. The behavior of β_K is of particular interest. β_K is expected to increase with increasing H, as the alignment of the magnetic impurities freezes out spin-flip Kondo scattering events [65]. However, as far as we are aware, no prior work has experimentally examined this precise evolution. We thus consider this determination of $\beta_K(H)$ an important dataset for the future understanding of the Kondo effect and its relationship with spin transport, and we believe it represents a future challenge to theory to accurately model this observed dependence.

F. Field dependence of the effective current polarization, $\alpha_{\rm eff}$

Before concluding, as an additional consistency check we consider the behavior of the effective current polarization, $\alpha_{\rm eff}(H, T)$, as shown in Fig. 5(d). The $\alpha_{\rm eff}(T)$ data for Cu/Al IL/Fe are also shown here (green diamonds). In the absence of Kondo scattering, $\alpha_{\rm eff}$ should approach a constant on cooling, as in the Al IL device. In the Cu/Fe device, however, this is not the case at small fields: As in the λ_N data, a downturn in $\alpha_{\rm eff}$ is seen at low temperatures, due to Kondo scattering through interdiffused MIs near the NM/FM interface, which is known to suppress the injected spin polarization [44]. Once again, however, the application of a magnetic field removes this suppression, as clearly shown in Fig. 5(d). By $\mu_0 H = 5$ T, $\alpha_{\rm eff}(T)$ is in fact approximately restored to that in the Al IL device. In Ref. [44], some of us showed that this $\alpha_{\rm eff}$ suppression is described by

$$\alpha_{\rm eff} = \alpha\left\{1 - z\left[\frac{1+\frac{2}{\beta_K}\frac{\tau_s'}{\tau_e'}}{\lambda_N} - \frac{\frac{2}{\beta_K}\frac{\tau_s'}{\tau_e'}}{\lambda_N + \frac{\rho_F}{(1-\alpha^2)\rho_N}\lambda_F}\right]\frac{\tau_e'}{\tau_{e,K}}\right\} \tag{7}$$

where z is the characteristic interdiffusion depth of the magnetic impurities in the NM channel, which is expected to be of the order of tens of nm for Cu/Fe [42], and τ_e' and τ_s' are the MI-free momentum and spin relaxation times, respectively. $1/\tau_e'$ and $1/\tau_s'$ were obtained using $1/\tau_e' = 1/\tau_e - 1/\tau_{e,K}$ and $1/\tau_s' = 1/\tau_s - 1/\beta_K\tau_{e,K}$, where $1/\tau_e$ and $1/\tau_s$ are determined from ρ_N and λ_N, while $1/\tau_{e,K}$ and β_K are the best fit values shown in Fig. 5(c). This leaves z and the intrinsic spin polarization α as the only free parameters in fits. The resulting best fit curves, shown by the solid lines in Fig. 5(d), reproduce the $\alpha_{\rm eff}$ data well. The extracted values of $\alpha = 0.4 \pm 0.04$ and $z = 57 \pm 24$ nm across the data set are also entirely plausible, and comparable to values obtained in Ref. [44].

It is evident from these results that the field-dependent background effects in $R_{\rm NL}$ can be understood as the suppression of Kondo scattering in the NM channel. Moreover, by extracting $1/\tau_s$ and $\alpha_{\rm eff}$ from the $R_{\rm spin}(d, T)$ data, the suppression of the Kondo scattering can be effectively modeled by the use of Eqs. (6) and (7). This has clear implications for NLSV devices based on materials that host MIs and hence have τ_s and $\alpha_{\rm eff}$ reduced by Kondo scattering. This effect is also likely to be present in more complicated systems, such as those where MIs have been intentionally introduced, or in complex heterostructures of Kondo active pairings. Here, relaxation from MIs could dominate and obscure spin lifetime measurements, e.g., through distortion of Hanle spin precession curves, due to the field dependence of both the saturation background and the spin lifetime. However, we have demonstrated in this work a simple means to quantify this effect, by application of a magnetic field large enough to saturate the moments.

G. Exchange field model

Due to the nature of our devices, which contain very low concentrations of dilute MIs, we discussed $R_{\rm spin}(H)$ above in terms of the physically relevant Kondo scattering regime. For completeness, however, we may also consider the impact of spin decoherence due to precession about a random exchange field, arising from MIs, such as those considered by McCreary *et al.* [51]. In such an exchange field model, the conduction electrons experience an exchange field from the impurity moments, with rms fluctuations ΔB_{ex}, about the average field $\overline{B_{ex}}$, occurring on a timescale τ_c, the correlation time. The spin relaxation rate due to this exchange field is given by [51,69]:

$$\frac{1}{\tau_{ex,s}} = \frac{(\Delta B_{ex})^2}{\tau_c}\frac{1}{\left(\mu_0 H + \overline{B_{ex}}\right)^2 + \left(\frac{\hbar}{g_e\mu_B\tau_c}\right)^2}, \tag{8}$$

where $\hbar$, g_e, and μ_B are Planck's constant, the electron g factor, and the Bohr magneton, respectively. Following the procedure in Ref. [51], we assume $\overline{B_{ex}}$ is described by a Brillouin function B_s through

$$\overline{B}_{ex} = \frac{cJS}{g_e\mu_B}B_S(\xi), \tag{9}$$

where $\xi \equiv Q/k_BT$, and $B_S(x)$ reduces to $\tanh(x)$ for spin $S = 1/2$ impurities.

We reproduce the spin relaxation rate as a function of temperature in Fig. 7(a), and now attempt to fit it with this exchange field model. ΔB and τ_c are expected to be independent of the magnetic field, but should vary with T, and we therefore fit $1/\tau_s(H)$ at fixed T using Eqs. (1), (8), and (9), with ΔB and τ_c as free parameters. [This is in contrast to the fitting procedure in Sec. III E, in which we fit $1/\tau_s(T)$ at fixed H.]

Although the exchange model appears to fit the data well, the extracted ΔB and τ_c are revealing. These are shown in Figs. 7(b) and 7(c), respectively, for $c = 100$ and 1000 ppm. We choose 1000 ppm here as this is close to the upper limit of a dilute system, and higher concentrations would be expected to lead to phase separation of Cu and Fe. Concentrations of 100 ppm and below are likely more representative of our devices, and we find that, at these concentrations, c has negligible impact on ΔB and τ_c, since $\overline{B_{ex}} \ll \mu_0 H$ in Eq. (8). Note that the 250 K ΔB and τ_c data have been excluded in Figs. 7(b) and 7(c), due to anomalously low and high values,

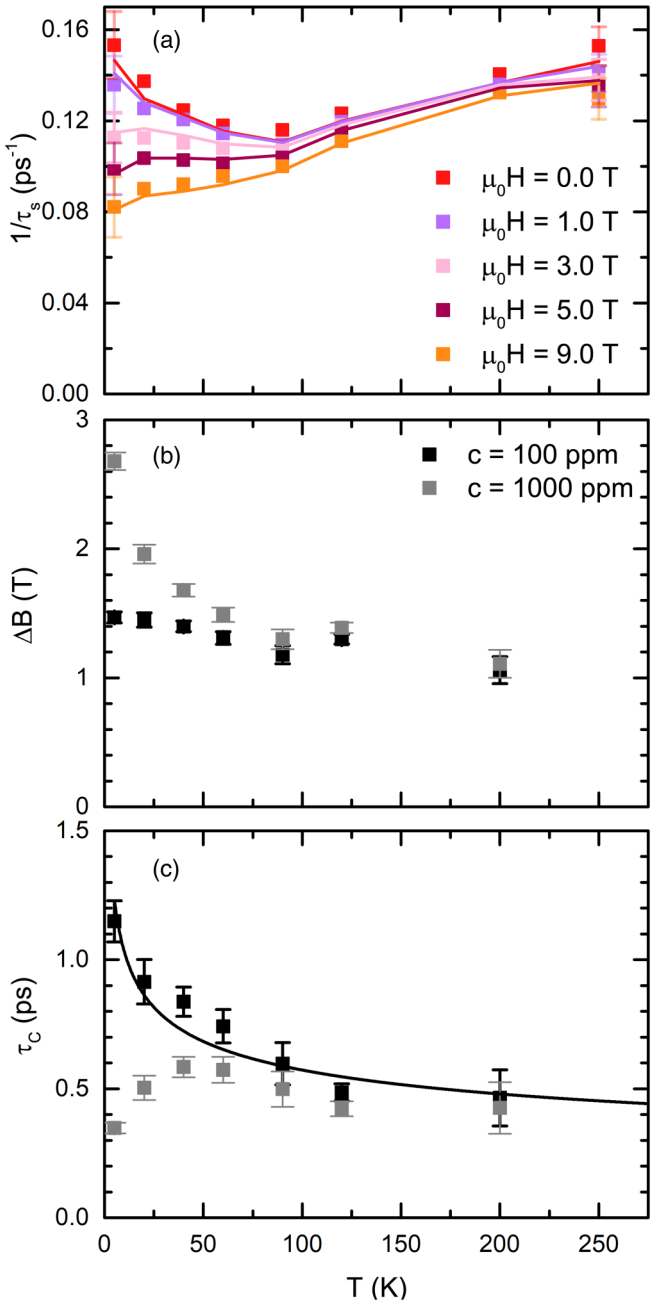

FIG. 7. (a) The $1/\tau_s$ data (squares) for Cu/Fe NLSVs fit using Eq. (8) (solid lines), in order to test the applicability of the exchange model. The data are the same as in Fig. 5(c). A reasonable agreement between the data and the fit is achieved. Parameters (b) ΔB and (c) τ_c extracted from the fitting in (a) for $c = 100$ and 1000 ppm, shown as a function of temperature. For $c = 100$ ppm, ΔB is independent of temperature, whereas τ_c increases with decreasing temperature, possibly indicating a spin-glass transition. Fitting using a conventional description for spin-glass dynamics [Eq. (10), solid line] reveals an unreasonably slow transition rate, however, indicating that a spin-glass transition does not suitably describe the system. $c = 1000$ ppm yields an unreasonably large ΔB and nontrivial T dependence of τ_c. Anomalous 250 K data in ΔB and τ_c (likely arising from the large spread in $1/\tau_s$) have been removed.

respectively, likely due to the large spread in the $1/\tau_s$ data at this temperature [Fig. 7(a)].

Looking first at the $c = 100$ ppm case, $\Delta B(T)$ is seen to fluctuate about a constant value of ~1.2 T. Although possible, such a large magnitude of ΔB is unlikely. τ_c also exhibits a strong temperature dependence, increasing with decreasing T, indicative of what would occur at a spin-glass transition, for example. It is generally expected that τ_c is constant in both NM and FM materials, changing dramatically only during a phase transition, e.g., spin-glass freezing [47,70–72]. Given the dilute nature of the MIs here, and so the weak inter-MI coupling, we do not believe that this T dependence can be physically realistic, particularly as we are far from the concentrations required for a spin-glass transition at this temperature ($c \sim 1\%$ for a transition at around 10 K in $Cu_{1-x}Fe_x$) [73,74].

Although unlikely, we nevertheless test the hypothesis of $\tau_C(T)$ indicating a spin-glass transition using the conventional description for the critical slowing down of spin dynamics in a spin glass [47,75]:

$$\tau_C = \tau_0 \left(\frac{T - T_g}{T_g} \right)^{-z\nu}, \tag{10}$$

where T_g is the spin-glass transition temperature, τ_0 is a characteristic timescale, and the exponent $z\nu$ is a constant. We fit the data using Eq. (10), with τ_0, T_g, and $z\nu$ as free parameters. The resulting fit, shown in Fig. 7(c), models the data reasonably, but fails to completely reproduce the form of $\tau_C(T)$. Moreover, the extracted parameters are $T_g \approx 0$ K and $z\nu = 0.25$. Such a $z\nu$ value is unfeasibly low [47], indicating that we are far from a transition at a (finite) T_g near 0 K. It is therefore unlikely that such a spin-glass transition is occurring in our devices.

Moving to the behavior of ΔB and τ_C at $c = 1000$ ppm , we find even less physical behavior, with ΔB increasing on cooling to a very large 2.7 T at 5 K, and τ_C varying non-monotonically with T. Such a strong temperature dependence of ΔB, and large magnitude, is clearly unreasonable. Hence, although the exchange model is able to fit the $1/\tau_s$ data, it is not able to provide satisfying physical insight into the T and H variation of $1/\tau_s$ (and thus δR_{NL}), as evidenced by the unreasonable T dependencies of ΔB and τ_C. We therefore conclude that the exchange model is not a suitable description for the field enhancement of R_{NL} we observe in our devices. We do emphasize, however, that this does not rule out such a mechanism becoming active in devices where the NM is (intentionally) more heavily substituted with MIs (thereby introducing MI-MI interactions) or directly exchange coupled to a FM [31]. There, it is reasonable to assume such exchange field coupling could be active. Indeed, should the materials in these devices undergo a magnetic phase transition, e.g., FM ordering or spin-glass freezing, then it is reasonable to expect this will also contribute to nonmonotonicity in $R_{spin}(H, T)$, potentially with comparable magnitudes to the Kondo scattering observed here. These could potentially be identified through the characterization of T_g and $z\nu$.

IV. CONCLUSION

An increase in nonlocal resistance in NLSVs under the application of an external magnetic field has been previously reported [6,26], and is observed here. Through the experimental measurement of a wide range of metallic NM/FM combinations, we demonstrate that the effect is correlated with the ability of the NM metal to host dilute magnetic impurity moments. Considering the field dependence of λ_N and $1/\tau_s$, we have shown that this strong field dependence originates from Kondo scattering in the NM channel, and that application of an external magnetic field quenches this scattering. We have successfully applied a model for Kondo scattering in a magnetic field to describe the spin-flip scattering rate data, demonstrating quantitative agreement with experiment and providing measurements of the field dependence of the Kondo EY parameter, $\beta_K(H)$. This work thus resolves the long-standing mystery of the origin of this high-field dependence, and points to a systematic underestimation of τ_s in NLSVs where MIs are present. Due to the low value of $\beta_K \sim 3/2$, this effect is significant, and is likely to be measurable in a variety of all-metallic NLSVs. By application of a magnetic field, however, we have demonstrated a simple means to remove the suppression and restore the nonlocal resistance to its Kondo-free value, obviating the need for additional material considerations or the inclusion of a diffusion-limiting interlayer.

ACKNOWLEDGMENTS

Work was supported by the UK EPSRC, Grant No. EP/P005713/1, and the National Science Foundation under Award No. DMR-1807124. Parts of this work were performed in the Characterization Facility, UMN, which receives partial support from NSF through the MSREC program. Other parts of this work were conducted in the Minnesota Nano Center, which is supported by the NSF through the National Nano Coordinated Infrastructure Network, under Awards No. NNCI-1542202 and No. ECCS-2025124.

[1] M. Yamada, D. Sato, N. Yoshida, M. Sato, K. Meguro, and S. Ogawa, IEEE Trans. Magn. **49**, 713 (2013).
[2] Y. K. Takahashi, S. Kasai, S. Hirayama, S. Mitani, and K. Hono, Appl. Phys. Lett. **100**, 052405 (2012).
[3] M. Takagishi, K. Yamada, H. Iwasaki, H. N. Fuke, and S. Hashimoto, IEEE Trans. Magn. **46**, 2086 (2010).
[4] M. Johnson and R. H. Silsbee, Phys. Rev. Lett. **55**, 1790 (1985).
[5] F. J. Jedema, A. T. Filip, and B. J. van Wees, Nature **410**, 345 (2001).
[6] G. Mihajlović, S. I. Erlingsson, K. Výborný, J. E. Pearson, S. D. Bader, and A. Hoffmann, Phys. Rev. B **84**, 132407 (2011).
[7] H. Idzuchi, Y. Fukuma, L. Wang, and Y. Otani, Appl. Phys. Lett. **101**, 022415 (2012).
[8] H. Zou and Y. Ji, Appl. Phys. Lett. **101**, 082401 (2012).
[9] S. Rakheja, S. C. Chang, and A. Naeemi, IEEE Trans. Electron Devices **60**, 3913 (2013).
[10] E. Villamor, M. Isasa, L. E. Hueso, and F. Casanova, Phys. Rev. B **88**, 184411 (2013).
[11] E. Villamor, M. Isasa, L. E. Hueso, and F. Casanova, Phys. Rev. B **87**, 094417 (2013).
[12] S. Chen, H. Zou, C. Qin, and Y. Ji, Appl. Phys. Express **7**, 113001 (2014).
[13] J. T. Batley, M. C. Rosamond, M. Ali, E. H. Linfield, G. Burnell, and B. J. Hickey, Phys. Rev. B **92**, 220420(R) (2015).
[14] Y. Cai, Y. Luo, C. Zhou, C. Qin, S. Chen, Y. Wu, and Y. Ji, J. Phys. D: Appl. Phys. **49**, 185003 (2016).
[15] F. J. Jedema, M. S. Nijboer, A. T. Filip, and B. J. van Wees, Phys. Rev. B **67**, 085319 (2003).
[16] S. O. Valenzuela and M. Tinkham, Appl. Phys. Lett. **85**, 5914 (2004).
[17] Y. Ji, A. Hoffmann, J. S. Jiang, and S. D. Bader, Appl. Phys. Lett. **85**, 6218 (2004).
[18] S. Garzon, I. Žutić, and R. A. Webb, Phys. Rev. Lett. **94**, 176601 (2005).
[19] T. Kimura, T. Sato, and Y. Otani, Phys. Rev. Lett. **100**, 066602 (2008).
[20] X. J. Wang, H. Zou, and Y. Ji, Phys. Rev. B **81**, 104409 (2010).
[21] G. Mihajlović, J. E. Pearson, S. D. Bader, and A. Hoffmann, Phys. Rev. Lett. **104**, 237202 (2010).
[22] M. Erekhinsky, A. Sharoni, F. Casanova, and I. K. Schuller, Appl. Phys. Lett. **96**, 022513 (2010).
[23] N. Poli, M. Urech, V. Korenivski, and D. B. Haviland, J. Appl. Phys. **99**, 2004 (2006).
[24] A. Fert and P. M. Levy, Phys. Rev. Lett. **106**, 157208 (2011).
[25] Y. Otani and T. Kimura, Philos. Trans. R. Soc., A **369**, 3136 (2011).
[26] K. Výborný, G. Mihajlović, A. Hoffmann, and S. I. Erlingsson, J. Phys.: Condens. Matter **25**, 216007 (2013).
[27] K. S. Das, F. K. Dejene, B. J. van Wees, and I. J. Vera-Marun, Phys. Rev. B **94**, 180403(R) (2016).
[28] D. Rüffer, F. D. Czeschka, R. Gross, and S. T. B. Goennenwein, Appl. Phys. Lett. **99**, 142112 (2011).
[29] Y. Niimi, D. Wei, H. Idzuchi, T. Wakamura, T. Kato, and Y. C. Otani, Phys. Rev. Lett. **110**, 016805 (2013).
[30] C. Zhou, F. Kandaz, Y. Cai, C. Qin, M. Jia, Z. Yuan, Y. Wu, and Y. Ji, Phys. Rev. B **96**, 094413 (2017).
[31] P. K. Muduli, M. Kimata, Y. Omori, T. Wakamura, S. P. Dash, and Y. C. Otani, Phys. Rev. B **98**, 024416 (2018).
[32] M. Johnson and R. H. Silsbee, Phys. Rev. B **76**, 153107 (2007).
[33] F. L. Bakker, A. Slachter, J. P. Adam, and B. J. Van Wees, Phys. Rev. Lett. **105**, 136601 (2010).
[34] M. Erekhinsky, F. Casanova, I. K. Schuller, and A. Sharoni, Appl. Phys. Lett. **100**, 212401 (2012).
[35] A. Hojem, D. Wesenberg, and B. L. Zink, Phys. Rev. B **94**, 024426 (2016).
[36] F. Casanova, A. Sharoni, M. Erekhinsky, and I. K. Schuller, Phys. Rev. B **79**, 184415 (2009).
[37] S. Takahashi and S. Maekawa, Phys. Rev. B **67**, 052409 (2003).
[38] R. J. Elliott, Phys. Rev. **96**, 266 (1954).
[39] Y. Yafet, in *Solid State Physics* (Academic Press, New York, 1963), pp. 1–98.
[40] P. Monod and F. Beuneu, Phys. Rev. B **19**, 911 (1979).
[41] J. D. Watts, L. O'Brien, J. S. Jeong, K. A. Mkhoyan, P. A. Crowell, and C. Leighton, Phys. Rev. Mater. **3**, 124409 (2019).

[42] L. O'Brien, D. Spivak, J. S. Jeong, K. A. Mkhoyan, P. A. Crowell, and C. Leighton, Phys. Rev. B **93**, 014413 (2016).
[43] J. D. Watts, J. S. Jeong, L. O'Brien, K. A. Mkhoyan, P. A. Crowell, and C. Leighton, Appl. Phys. Lett. **110**, 222407 (2017).
[44] K. W. Kim, L. O'Brien, P. A. Crowell, C. Leighton, and M. D. Stiles, Phys. Rev. B **95**, 104404 (2017).
[45] K. Hamaya, T. Kurokawa, S. Oki, S. Yamada, T. Kanashima, and T. Taniyama, Phys. Rev. B **94**, 140401(R) (2016).
[46] L. O'Brien, M. J. Erickson, D. Spivak, H. Ambaye, R. J. Goyette, V. Lauter, P. A. Crowell, and C. Leighton, Nat. Commun. **5**, 3927 (2014).
[47] J. A. Mydosh, *Spin Glasses: An Experimental Introduction* (Taylor & Francis, London, 1993).
[48] G. Gruner and A. Zawadowski, Rep. Prog. Phys. **37**, 1497 (1974).
[49] J. Kondo, S. Koikegami, K. Odagiri, K. Yamaji, and T. Yanagisawa, *The Physics of Dilute Magnetic Alloys* (Cambridge University Press, Cambridge, 2012).
[50] S. P. Dash, S. Sharma, J. C. Le Breton, J. Peiro, H. Jaffrès, J.-M. George, A. L. Lemaître, and R. Jansen, Phys. Rev. B **84**, 054410 (2011).
[51] K. M. McCreary, A. G. Swartz, W. Han, J. Fabian, and R. K. Kawakami, Phys. Rev. Lett. **109**, 186604 (2012).
[52] S. Vélez, V. N. Golovach, A. Bedoya-Pinto, M. Isasa, E. Sagasta, M. Abadia, C. Rogero, L. E. Hueso, F. S. Bergeret, and F. Casanova, Phys. Rev. Lett. **116**, 016603 (2016).
[53] R. K. Bennet, A. Hojem, and B. L. Zink, Phys. Rev. B **100**, 104404 (2019).
[54] See Supplemental Material at http://link.aps.org/supplemental/10.1103/PhysRevB.104.014423 for further discussion on δR_{NL} and R_b in other material pairings and the isotropy of δR_{NL} with field direction, further discussion on Brillouin fits and Langevin fits to $\delta R_{\mathrm{NL}}/R_{\mathrm{spin}}$, and further discussion on fitting the spin relaxation rate with an alternative Kondo model.
[55] S. Takahashi and S. Maekawa, Phys. C (Amsterdam, Neth.) **437-438**, 309 (2006).
[56] J. Bass and W. P. Pratt, J. Phys.: Condens. Matter **19**, 183201 (2007).
[57] F. Beuneu and P. Monod, Phys. Rev. B **18**, 2422 (1978).
[58] K. Inoue and Y. Nakamura, Phys. Status Solidi **58**, 355 (1973).
[59] D. Goldhaber-Gordon, J. Göres, M. A. Kastner, H. Shtrikman, D. Mahalu, and U. Meirav, Phys. Rev. Lett. **81**, 5225 (1998).
[60] W. Wei and G. Bergmann, Phys. Rev. B **37**, 5990 (1988).
[61] P. Monod, Phys. Rev. Lett. **19**, 1113 (1967).
[62] E. W. Fenton, Phys. Rev. B **7**, 3144 (1973).
[63] V. I. Litvinov, Phys. Status Solidi **77**, 71 (1976).
[64] A. A. Abrikosov, Phys. Phys. Fiz. **2**, 61 (1965).
[65] H. Rohrer, Phys. Rev. **174**, 583 (1968).
[66] J. Kondo, Prog. Theor. Phys. **32**, 37 (1964).
[67] J. A. Appelbaum, Phys. Rev. **154**, 633 (1967).
[68] E. L. Wolf and D. L. Losee, Phys. Rev. B **2**, 3660 (1970).
[69] J. Fabian, A. Matos-Abiague, C. Ertler, P. Stano, and I. Zutic, Acta Phys. Slovaca **57**, 565 (2007).
[70] Y. J. Uemura, T. Yamazaki, D. R. Harshman, M. Senba, and E. J. Ansaldo, Phys. Rev. B **31**, 546 (1985).
[71] M. B. Salamon, Phys. Rev. **155**, 224 (1967).
[72] Y. Niimi, M. Kimata, Y. Omori, B. Gu, T. Ziman, S. Maekawa, A. Fert, and Y. Otani, Phys. Rev. Lett. **115**, 196602 (2015).
[73] T. Uchiyama, M. Matsui, and K. Adachi, IEEE Trans. Magn. **23**, 2305 (1987).
[74] D. Korn and G. Zibold, J. Phys. F: Met. Phys. **15**, 2497 (1985).
[75] M.-K. Hou, M. B. Salamon, and T. A. L. Ziman, Phys. Rev. B **30**, 5239 (1984).